RESEARCH ARTICLE | FEBRUARY 05 2024

Reconfigurable spin wave modes in a Heusler magnonic crystal FREE

S. Mantion ; A. Torres Dias ; M. Madami ; S. Tacchi ; N. Biziere ✉

Check for updates

View Online   Export Citation   CrossMark

Reconfigurable spin wave modes in a Heusler magnonic crystal

S. Mantion,[1] A. Torres Dias,[2] M. Madami,[3] S. Tacchi,[4] and N. Biziere[1,a)]

AFFILIATIONS

[1]CEMES-CNRS, Université de Toulouse, 29 rue Jeanne Marvig, Toulouse 31055, France
[2]LPCNO, INSA-CNRS-UPS, Université de Toulouse, 135 Av. Rangueil, 31077 Toulouse, France
[3]Dipartimento di Fisica e Geologia, Università di Perugia, I-06123 Perugia, Italy
[4]Istituto Officina dei Materiali del CNR (CNR-IOM), Sede Secondaria di Perugia, c/o Dipartimento di Fisica e Geologia, Università di Perugia, I-06123 Perugia, Italy

[a)]Author to whom correspondence should be addressed: nicolas.biziere@cemes.fr

ABSTRACT

We report on the field evolution of the microwave spin wave modes in magnonic crystals made of square antidot lattices etched in a thin film of the Co_2MnSi Heusler alloy and having a lateral size s of 200 nm and an edge-to-edge separation d of 600 or 800 nm. The spin wave modes are investigated combining ferromagnetic resonance, Brillouin light scattering experiments, and micromagnetic simulations of the static and dynamic magnetic states as a function of the applied field. We show that for applied fields ≥ 10 mT, when the magnetization is quasi-saturated across the crystals, the two samples show similar behavior and the two most intense modes in the spin waves spectra correspond to a mode extending in the channels comprised between the antidot and a mode localized in the region between the antidots. For smaller fields, we observe a difference of the measured spectra as a function of d. This is attributed to the fact that for $d = 800$ nm, the magnetization remains partially uniform in the channel between the antidots because of the Heusler cubic crystal anisotropy, while for $d = 600$ nm, the magnetic edge domains around the antidots spread into the channels. Moreover, this anisotropy also allows different remanent states when initializing the crystals with a small magnetic field along two perpendicular directions. This leads to an efficient excitation or extinction of the spin wave modes, making possible to achieve reconfigurable microwave devices exploiting an antidot geometry in a metallic ferromagnetic with a low damping coefficient.

I. INTRODUCTION

Magnonics is a field that involves the processes of exciting, manipulating, and detecting spin waves (SWs) in a magnetic medium. Its potential applications are extremely wide-ranging, among which are information and beyond CMOS technologies, neuromorphic computing, logic devices, passive components, and magnetic sensors, to name a few.[1–10] In particular, SWs in ferrimagnets, ferromagnets, and antiferromagnets offer many advantages. For example, their frequencies can range from a few hundreds of MHz to THz for wave vectors ranging from millimeters to nanometers.[11,12] This offers good perspectives to develop low energy consumption devices for on-chip integration. Moreover, the magnetic nature of the medium allows for long lifetime applications, frequency or wave vector tuning with an external magnetic field, or reconfigurable operations[13] among other advantages.

Magnonic crystals (MCs) are a class of magnonic devices consisting of magnetic materials with a periodic modulation of one or several magnetic properties such as magnetization, internal field, or anisotropy. This can be achieved by a modulation of the geometrical parameters (dots and antidots,[14–17] thickness or width modulation in thin films[18,19]), the magnetic parameters (bicomponent[20–23] or ion implanted structures[24]), the applied magnetic field,[25] the local strain,[26] and the magnetic texture.[27,28] Also, MCs offer a great playground for fundamental studies of SWs in confined structures and particularly interesting phenomena such as SW stopbands, also called frequency bandgaps.[29–31]

MCs have now become an intense field of research, and already some devices have been demonstrated for microwave filtering, delay lines, or data processing.[32–34] Also, they are highly suitable to make passive microwave devices because their bandgaps

and operating frequencies can be easily tuned by the geometrical parameters of the lattice. For components such as microwave filters, the properties sought for the materials are (i) a low damping coefficient to obtain a long SW propagation distance and (ii) high magnetization values to operate at frequencies up to a few GHz (notably for telecommunications technologies) and reach large frequency bandgaps.[35,36] For nanoscale integration, the device is expected as well to work at remanence, which means without the need for permanent magnets, and to be compatible with nanofabrication processes. Finally, the search for reconfigurable operations at remanence, i.e., the possibility of obtaining on demand different microwave responses, has become highly desirable to improve the functionalities of the devices.[37–43]

The Co_2MnSi (CMS) full Heusler alloy is very attractive in fulfilling all the aforementioned requirements. In particular, it is a half-metal ferromagnet leading to a small Gilbert-like damping coefficient α below 10^{-3}.[44–47] Even if this is still one or two orders of magnitude higher than YIG ferrites, this material is also noted for its high magnetization value ($\approx 5\,\mu_B$/f.u, $\mu_0 M_s \approx 1.3$ T)[48,49] and spin polarization, above 90% experimentally[46,50,51] allowing to combine magnonic and spintronic functionalities.[2,52] In addition, CMS shows a high Curie temperature (around 985 K)[53,54] and a relatively high cubic crystal anisotropy ($\mu_0 H_k \approx 20$–30 mT), which were predicted to allow reconfigurable SW modes at remanence in antidot lattices.[48,55] However, to our knowledge, only a few magnonics studies have been performed up to now with such materials and few Co-based Heusler alloy magnonic crystals exist in the literature.[56–62]

In this work, we report a systematic investigation of the SW modes in two magnonic crystals made of squared antidot lattices, etched from a thin CMS film, and having a lateral size $s = 200$ nm and an edge-to-edge separation $d = 600$ or 800 nm. The evolution of the SW modes as a function of the intensity of the external magnetic field applied along a side of the antidot arrays, was studied combining broadband ferromagnetic resonance and micro-focused Brillouin light scattering (micro-BLS) measurements. Micromagnetic simulations of the SW frequencies at different applied field values are found to be in very good agreement with the measurements of SW spectra for both crystals, even at low fields for which the magnetization shows non-uniformities. In addition, micro-BLS mapping of the main SW modes confirms the spatial profiles obtained in the simulations for the modes with the largest intensity. Finally, for $d = 800$ nm, we show that the cubic anisotropy allows to stabilize quasi-uniform remanent states when the field is applied in two directions perpendicular to each other, leading to a highly pronounced extinction of the SW modes for reconfigurable operations.

II. METHODS

A thin film of CMS with a thickness of 45 ± 2 nm is deposited on a (100)-oriented MgO crystal substrate by magnetron sputtering with a base pressure of 2×10^{-8} mbar. The layer is deposited at 500 °C with a speed of approximately 1 nm/min and annealed at 700° for 2 h. This procedure favors the $L2_1$ order of CMS.[48,55,63] This reference sample is then cut into several pieces.

The antidot lattices are then realized in two steps. First, the lattice of squares is patterned in a mr-POS EBR 0.3 resist by
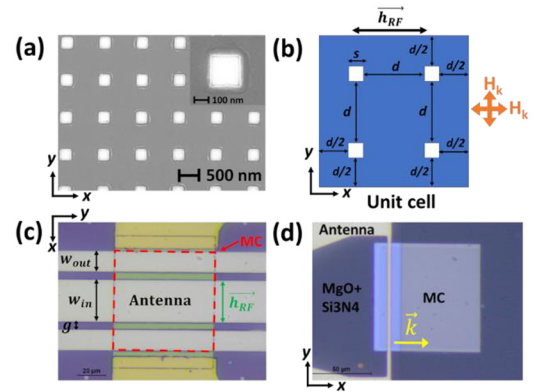
FIG. 1. (a) SEM images of a CMS squared antidot array with $s = 200$ nm and $d = 600$ nm. (b) A schematic of a unit cell used for micromagnetic simulations. 2D periodic boundary conditions are used in the x and y directions. The directions of the CMS cubic anisotropy axes are shown in orange. (c) and (d) Optical images of the micro-antennas used for field-sweep or frequency-sweep FMR measurements (c) and for BLS experiments (d). The wave vector direction of the propagating SWs in BLS experiments is shown in yellow.

electron beam lithography. The dimension of the lattice is $70 \times 70\,\mu m^2$. Then, the pattern is transferred in the CMS film by Ar^+ ion beam etching in a dedicated ion beam etching chamber. An example of a square antidot pattern is shown in Fig. 1(a). The nominal lateral size s is 200 ± 10 nm and the separation d is 600 ± 10 and 800 ± 10 nm for the first and second samples, respectively. Let us note that the antidots have more rounded edges for the sample with $d = 800$ nm (images not shown here). Once the antidot lattice is made, it is separated from the rest of the CMS layer by Ar^+ ion etching all around the MC on an area of approximately $800 \times 800\,\mu m^2$. Finally, a micro-antenna is deposited on top of the MC. Two kinds of antennas, one for ferromagnetic resonance (FMR) and one for micro-BLS experiments, are realized by LASER UV-lithography, followed by a lift-off of $Ti_{10nm}/Cu_{200nm}/Au_{30nm}$.

Broadband FMR experiments are performed to measure the evolution of the resonance frequencies as a function of the external magnetic field. They are performed using the micro-antenna shown in Fig. 1(c) corresponding to a portion of a coplanar waveguide shorted at one end. The micro-antenna covers the surface of the MC and is insulated from the MC by an $a \approx 200$ nm thick Si_3N_4 passivation layer deposited by magnetron sputtering. The width of the central and outer conductors is $w_{in} = 30$ and $w_{out} = 15\,\mu m$, respectively, and the gap is g = $5\,\mu m$.

The large central conductor allows for a microwave pumping field h_{RF} with a very small k vector such as $k_{max} \approx 2\pi/w_{in} = 0.209$ rad μm^{-1}. In order to evaluate the frequency shift induced by the non-zero wave vector with respect to the FMR mode (i.e., $k = 0$ rad μm^{-1}), we calculated the $f(k)$ dispersion curves for stripes of width 600 and 800 nm according to the Slavin–Kalinikos theory.[3,38,64] We obtained a maximum shift of approximately 30 MHz for the mode $n = 1$ and an even less shift for the modes with a higher quantization number n. Therefore, we consider in the

following that we are close to obtaining the FMR configuration, which normally implies a uniform h_{RF} over the sample.

Two different configurations were used in the FMR experiments, which are referred to as field-sweep or frequency-sweep FMR measurement in the following. In field-sweep FMR experiments, the external magnetic field H_0 is swept from 300 to 0 mT, while keeping the frequency of h_{RF} constant. The antenna is connected with a non-magnetic microwave picoprobe (Southwest Factory) to an Agilent microwave source (0.1–30 GHz). The microwave reflected signal from the antenna passes through a circulator and a microwave diode connected to a lock-in amplifier. The excited SW modes are then detected by synchronous detection as the variation of microwave power absorbed by the MC at the resonance field. For this, the applied field H_0 is modulated with an amplitude of 0.2 mT at a frequency of 113 Hz.

For frequency-sweep FMR measurements, the microwave frequency $\omega_{RF}/2\pi$ of the pumping field is swept, while keeping a constant H_0 value. Here, the antenna is connected to a 0.1–20 GHz Anritsu Vectorial Network Analyzer (VNA). The spin wave spectra are measured as the difference $\Delta S_{11} = S_{11}(H_0) - S_{11}(ref)$, where $S_{11}(H_0)$ is the reflected signal from the antenna at a particular value of H_0 and $S_{11}(ref)$ is the reflected signal measured at $\mu_0 H_0 = 350$ mT for which the spin wave spectrum is above 20 GHz. Frequency and field-sweep measurements are performed with a microwave power set at −20 dBm on the generator output and H_0 is applied either in the x or in the y directions.

Micro-BLS is exploited to image the intensity of the SW modes. Micro-BLS measurements are performed by focusing a single-mode solid-state laser (with a wavelength of 532 nm) at normal incidence onto the sample surface using an objective with a numerical aperture of 0.75, giving a spatial resolution of approximately 250 nm. A (3 + 3)-pass tandem Fabry–Pérot interferometer is used to analyze the inelastically scattered light. A nanopositioning stage allows us to position the sample with a precision down to 10 nm on all three axes. The strip line antenna shown in Fig. 1(d) and having a width of 2.5 μm, is fed with an electrical probe station ranging from dc up to 20 GHz to excite SWs. The antenna is isolated from the MC by an $a \approx 150$ nm thick Si_3N_4 passivation layer [light blue in Fig. 1(d)], while the rest of the MC is passivated with only a 50 nm thick layer. The microwave power is set at +16 dBm on the microwave generator output. Micro-BLS measurements are carried out in Damon–Eshbach (DE) geometry applying a magnetic field along the y direction, i.e., parallel to the antenna.

In order to explain the evolution of the SW spectra as a function of H_0, we used Mumax3[65] to perform micromagnetic simulations of the equilibrium magnetic states and dynamic SWs modes of the squared antidot lattices with the geometry shown in Fig. 1(b). The unit cell is divided in cubic cells with dimensions of $5 \times 5 \times 5$ nm^3, below the exchange length of CMS , as defined in Ref. 66. To set the magnetic parameters in the simulations, we used the one obtained from FMR measurements (not shown here) performed on a piece of the CMS reference thin film. We obtained the saturation magnetization $\mu_0 Ms = 1.28$ T, the exchange constant $A = 21 \times 10^{-12}$ J/m, the cubic crystal anisotropy constant $K = 10.1 \times 10^3$ J/m^3 $(\mu_0 H_k \approx 21$ mT), the gyromagnetic ratio $\gamma = 28.8$ GHz/T, and the Gilbert damping coefficient $\alpha = 2 \times 10^{-3}$. Let us note that we measured an extrinsic contribution to the

linewidth $\Delta H_0 = 2$ mT, which is not considered in the simulations. The film thickness is 45 nm. We used 2D periodic boundary conditions (PBC) in order to simulate an infinite MC.

The equilibrium state is calculated at particular values of H_0. We apply the field with a 1° misalignment with respect to the symmetry axes (x or y) of the MC to reproduce the uncertainty of alignment for H_0 in the experiment. Once the equilibrium state is reached, the system is left to relax for 10 ns defining the initial remanent state used as the starting point for dynamic simulations.

To calculate the frequencies of the SW modes, we applied a spatially uniform magnetic pulse along the x axis with a temporal *Sinc* form. The cutting frequency of the pulse is 30 GHz. The amplitude of h_{RF} is 1 mT, which ensures it to be in the linear regime of SW excitation. We then recorded 2048 magnetization files with a time step of 10 ps. This leads to a Nyquist frequency of 50 GHz. To obtain the SW spectra, a Fast Fourier Transform (FFT) is performed on the time varying z component of the magnetization $M_z(t)$ averaged over all cells.

The SW profiles is also calculated in the plane $z = 45$ nm (top surface of the MC). To do this, the initial equilibrium remanent state is first subtracted to each temporal magnetic file. Then, FFT and inverse FFT are performed for each cubic cell to, respectively, filter a particular frequency and recover the corresponding time evolution of the dynamic magnetization component in the direction of h_{RF}, i.e., the m_x component. The spin wave profiles shown in Figs. 3, 4, and 8 correspond to the snapshots at the time τ for which the amplitude of the $m_x(\tau)$ component averaged over all cells is maximum.

## III. RESULTS

A. Spin wave modes in quasi-saturated states

Figures 2(a) and 2(b) present field-sweep FMR measurements for the sample with $d = 800$ and 600 nm, respectively. H_0 is applied along the y direction, parallel to the length of the micro-antenna [see Fig. 1(c)]. The intensity of the microwave absorption signal as a function of $\omega_{RF}/2\pi$ and H_0 is color coded in gray scale, while top panels show examples of line cuts of the signals recorded at 15 GHz as a function of H_0.

Many absorption peaks, corresponding to the different SWs modes excited by the micro-antenna, are observed for both samples. Moreover, the two samples exhibit a similar behavior when $\mu_0 H_0 \geq 10$ mT (the case $0 \leq \mu_0 H_0 < 10$ mT will be discussed in Sec. III C). In particular, two main signals, having large amplitudes and referred to as mode A and mode B for the highest and lowest frequency peaks, respectively, are found in the whole investigated field range. We also observe an increasing number of low frequency modes as H_0 increases.

These findings are very well reproduced by the micromagnetic simulations, as can be seen in Figs. 2(a) and 2(b), where the simulated frequencies are reported by colored symbols for the sample with $d = 800$ and 600 nm, respectively. Their corresponding calculated spatial profiles (i.e., snapshots of the dynamic m_x amplitude) are presented in Figs. 3 and 4, where the modes with the highest calculated amplitudes are surrounded by black dotted lines.

As can be seen, the calculated spatial profiles of the different SW modes show a marked evolution as a function of the field

19 February 2024 13:16:43
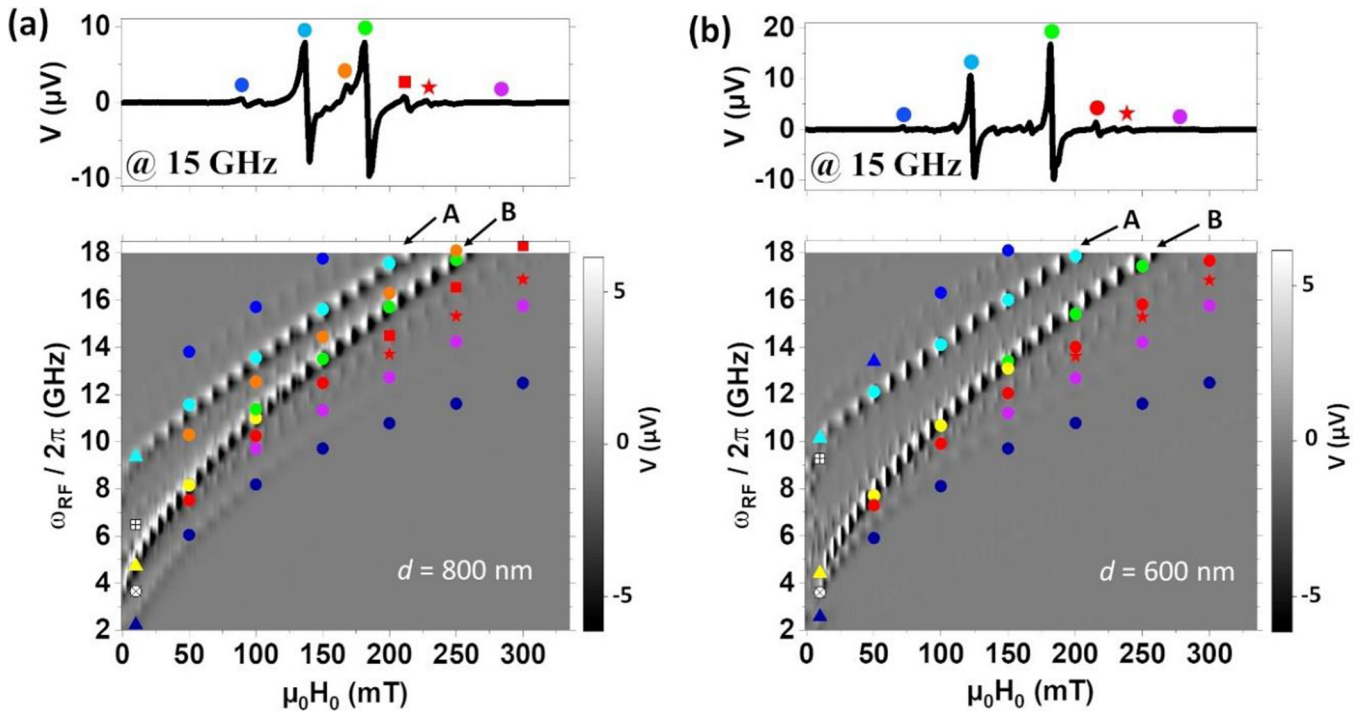
FIG. 2. Field-sweep FMR measurements for the sample with d = (a) 800 and (b) 600 nm. The amplitude of the lock-in signal in (a) and (b) is color coded according to the color bar on the right. An example of the signal recorded at 15 GHz as a function of H_0 is shown on the top of the images. The colored symbols in (a) and (b) correspond to the calculated spin wave modes whose spatial profiles are shown in Figs. 3 and 4, respectively.

amplitude because of the changes in the equilibrium magnetic state. In particular, two equilibrium states, i.e., the quasi-saturated state for $\mu_0 H_0 \geq 50$ mT and the intermediate states for 10 mT $\leq \mu_0 H_0 < 50$ mT can be defined. In the quasi-saturated state, the edge domains around the antidots are very small and show a butterfly shape. Also, the magnetization in the horizontal channels is almost fully saturated in the direction of H_0. Instead, in the intermediate state, the size of the edge domains increases, spreading into the horizontal channels. In addition, their shape evolves with a rotation of the magnetization along the x direction because of the local shape anisotropy induced by the antidot.

From a comparison between experiments and simulations, we deduce that mode A observed in the field-sweep FMR measurements corresponds to localized modes (turquoise circle and triangle), having maximum precession amplitude between the antidots. In the quasi-saturated state, this mode is characterized by a periodic pattern in the horizontal channels comprised between antidots, having a periodicity of approximately d along the x and y directions. In the intermediate state, this mode exhibits a more complex spatial profile with several oscillations in the horizontal channels. Mode B, instead, corresponds to extended modes (green and yellow circles, yellow triangle) characterized by a quasi-uniform magnetization precession amplitude within the horizontal channels comprised between rows of antidots. The spatial distribution of the magnetization precession for modes A and B explains their strong

FMR signal because most of the magnetic volume oscillates in phase, leading to a large coupling with h_{RF}. Similar extended and localized modes have been reported in previous experiments performed in antidot lattices made of Permalloy, for example.[67–73]

It is interesting to note that the spatial profile of mode B has a more pronounced field dependence than that of mode A. Indeed, at a high field, mode B shows a non-zero oscillation amplitude in between the antidots, with a π dephasing with respect to the magnetization in the horizontal channel (see the green circle mode, for example). When H_0 decreases, the oscillation amplitude between the antidots is reduced and the magnetization precession remains in the horizontal channel (yellow circle). Interestingly, such transformation from the green to the yellow circle mode occurs at 100 and 150 mT for $d = 800$ and 600 nm, respectively. This can be explained by observing that when d decreases, it is more difficult to saturate the magnetization along the y direction between the antidots due to a more important contribution of the local demagnetizing field. Finally, in the intermediate state, one can observe for both samples that the region of quasi-uniform magnetization precession becomes confined in a narrower region comprised between edge domains where the precession amplitude is large and out of phase by π (yellow triangle).

The simulations indicate that for both d values, the mode observed at the highest frequency (represented by blue circle and blue triangle modes) in the quasi-saturated state corresponds to
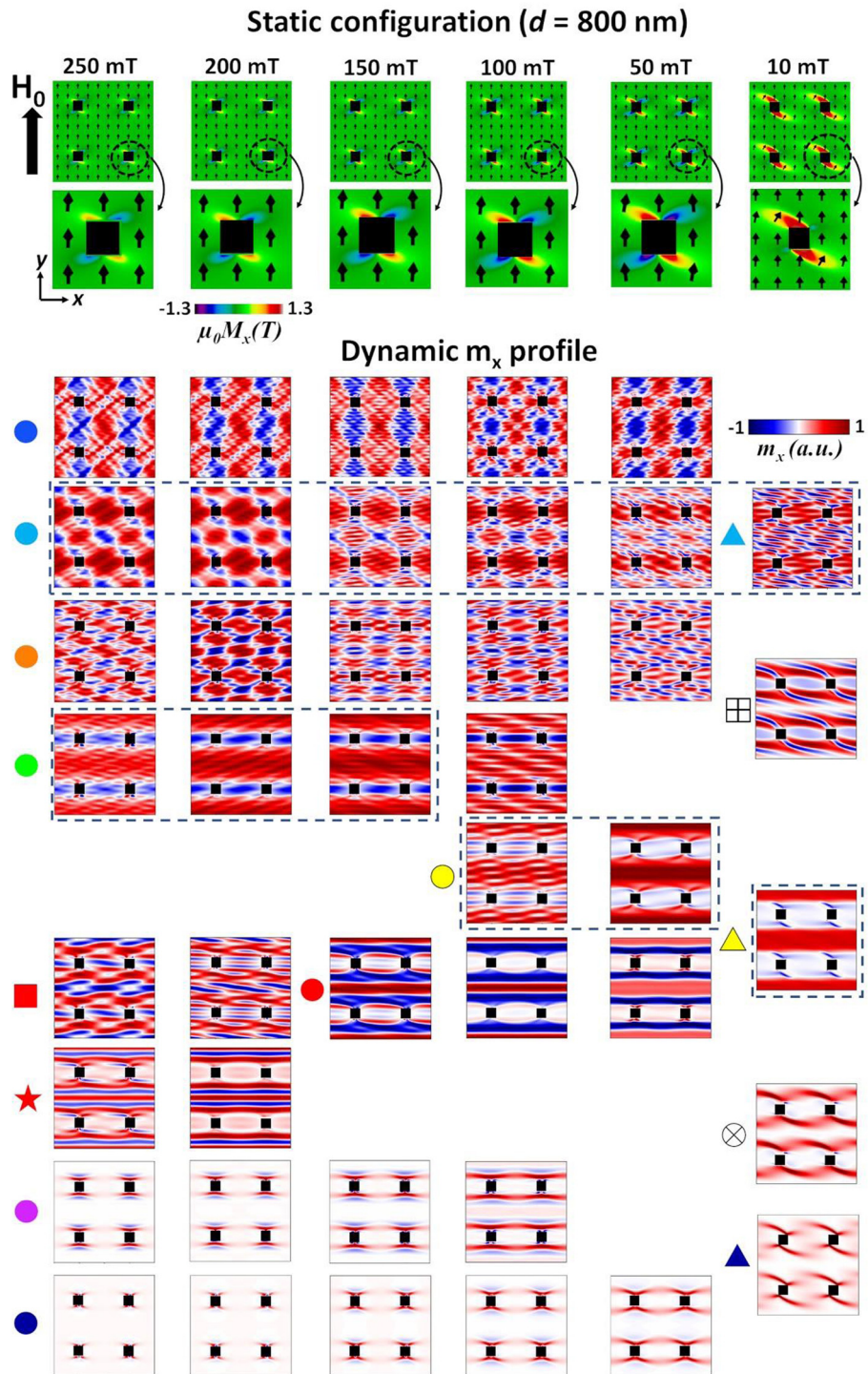
FIG. 3. Micromagnetic calculations of the equilibrium magnetic states and spatial profiles of the dynamic modes for a MC with $s = 200$ nm and $d = 800$ nm. Each column shows, from the top to the bottom, the equilibrium magnetic state and the dynamic m_x components calculated as described in Sec. II. Below each equilibrium magnetic state, a zoom around one antidot is shown as an example to observe the magnetization distribution in the edge domain. The colored symbols describe the different spin wave modes and are the same as in Fig. 2(a). Antidots are schematically shown by black squares.
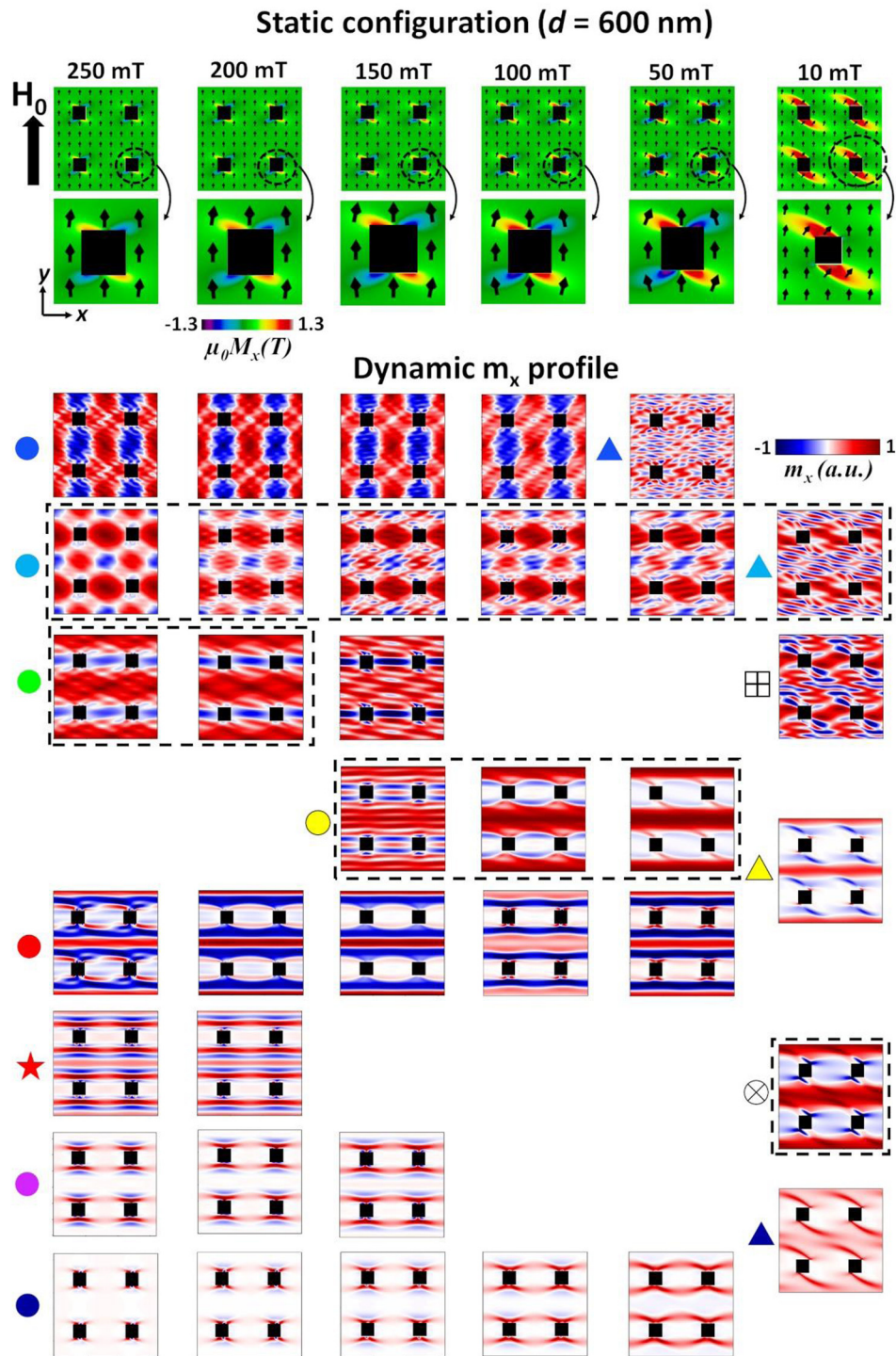
FIG. 4. Micromagnetic calculations of the equilibrium magnetic states and spatial profiles of the dynamic modes for a MC with $s = 200$ nm and $d = 600$ nm. Each column shows, from the top to the bottom, the equilibrium magnetic state and the dynamic m_x components calculated as described in Sec. II. Below each equilibrium magnetic state, a zoom around one antidot is shown as an example to observe the magnetization distribution in the edge domain. The colored symbols describe the different spin wave modes and are the same as in Fig. 2(b). Antidots are schematically shown by black squares.

localized SW modes showing a periodic pattern along the x and y directions with a periodicity of approximately d in both directions. In the intermediate state, these modes are observed to disappear because of a modification of the static magnetic configuration. Moreover, the simulations reproduce the presence for high field values of additional modes at frequencies below the main peak B. They correspond to the red and violet circles and red square and red star modes, which can be considered as extended modes along the x direction.

The red circle and red star modes can be compared with quantized modes in stripes geometrically defined by the uniformly magnetized region confined between edge domains, showing 3 and 5 antinodes along y, respectively. However, the analogy with stripes is not straightforward since a strong precession is also observed inside (the red circle at $\mu_0 H_0 = 50$ mT, red star) or in between (the red circle at $\mu_0 H_0 \geq 100$ mT) the edge domains. Such a complex spatial structure leads to a small signal amplitude both experimentally and in the simulations since the spatially averaged dynamic components tend to cancel each other. For $d = 800$ nm, when increasing the amplitude of H_0, the red circle turns into a red square mode, which shows an even more complex structure along x.

For the mode described by the violet circle, the magnetization precession is strong in a narrow channel localized very close to the antidots, and it becomes more and more confined and localized around the antidots when increasing H_0. Such a feature explains why its experimental signature becomes less and less visible at a high field because of the weak coupling with the antenna. Also, its peculiar spatial profile make this mode highly sensitive to the geometrical imperfections of the antidots where small variations of shapes and sizes induce large resonance frequency shifts and a broadening of the peaks.[74] Similar arguments can explain the disappearance at high fields of the edge modes localized in the edge domains and represented by the dark blue circle mode in the simulations. In contrast, one can notice that the experimental signal of this mode becomes stronger when decreasing H_0. This is because there is a larger magnetization volume that oscillates, not only inside the larger edge domains but also between antidots, as shown by the modes described by the dark blue triangle.

Note that the only noticeable difference between $d = 800$ and 600 nm for the calculated SW spectra in the quasi-saturated state is the presence of an additional mode for $d = 800$ nm lying between modes A and B. This mode is described as an orange circle in Figs. 2(a) and 3. Simulations reproduce the evolution of its frequency position, which tends to be closer from the main peak A (B) at a low (high) field. Because of its complex spatial structure, it is not obvious to define whether it is more of an extended or localized mode. Nevertheless, it is also periodic along the x and y directions, with a periodicity of approximately d along x and $d/2$ along y.

Finally, one can observe that in the intermediate state, there is the appearance of new modes described as crosses surrounded by a circle or a square. As can be seen, their spatial profiles are impacted by the presence of edge domains. Even if the experimental intermediate state is obviously dependent on the local geometrical inhomogeneities of the antidots, we still observe a very good agreement between the experimental FMR measurements and the simulated SW modes for both samples.

B. BLS spectra and mapping of spin waves in quasi-saturated states

In order to complement micromagnetic simulations and FMR experiments, a two-dimensional imaging of the SW modes in the quasi-saturated equilibrium state was carried out for both samples by means of micro-BLS to study the evolution of the SWs' spatial profile as a function of the geometrical parameters and the intensity of the applied field.

First, micro-BLS measurements were performed measuring the SW intensity as a function of excitation frequency in the range between 2 and 16 GHz. BLS spectra recorded applying an external field $\mu_0 H_0 = 100$ and 50 mT for the samples with $d = 800$ and 600 nm are reported in panels (a) and (d) of Figs. 5 and 6, respectively. For both samples, the BLS spectra show two intense peaks and a less intense peak at a lower frequency.

When the external field is reduced, all the three peaks are observed to shift at lower frequencies. Note that the measured BLS frequencies of the most intense peaks agree very well with those in frequency-sweep FMR measurements [panels (b) and (e) of Figs. 5 and 6] and in the calculated SW spectra [panels (c) and (f) of Figs. 5 and 6].

Then, for the two most intense modes, a 2D map of the BLS intensity was acquired at a fixed frequency over an area of approximately $5 \times 5 \, \mu m^2$ with a 250 nm step size. Such mappings are shown at the top of panels (a) and (d) of Figs. 5 and 6. As can be seen, the higher frequency mode always corresponds to a localized mode, having the largest amplitude in the region comprised between the antidots, while the lower frequency mode corresponds to an extended mode propagating in the horizontal channels, perpendicularly to the external field (DE configuration), in good agreement with the calculated spatial profiles of the modes described by the yellow and turquoise circles. Moreover, from the comparison between the experimental BLS spectra and the micromagnetic simulations, the peak at the lower frequency can be labeled as an edge mode (dark blue circle). However, due to the small lateral size of the antidots, the spatial localization of this mode cannot be resolved in the two-dimensional micro-BLS maps.

In agreement with previous studies, both BLS and frequency-sweep FMR measurements demonstrate that the variation of dipolar energy with d has an opposite effect depending on the mode spatial localization. For the extended mode, the frequency is higher in the sample with $d = 800$ nm, while for the localized mode, it is higher for $d = 600$ nm. As a consequence, the frequency difference between the extended and the localized modes increases when decreasing d, as was already clearly observed in Fig. 2. This opposite trend as a function of the aspect ratio t/d (thickness over the width of the channels comprised between the antidots) has been ascribed to the fact that the extended modes can be considered as the resonances of transversely magnetized horizontal channels, whereas the localized mode is the lowest resonant mode of longitudinally magnetized vertical channels.[75]

Figure 7 shows the evolution of the BLS intensity of the extended mode recorded as a function of the distance from the antenna and for the two values of d. In order to take into account the variations of the SW propagation in the different regions of the sample, we record the signal at the center of the horizontal
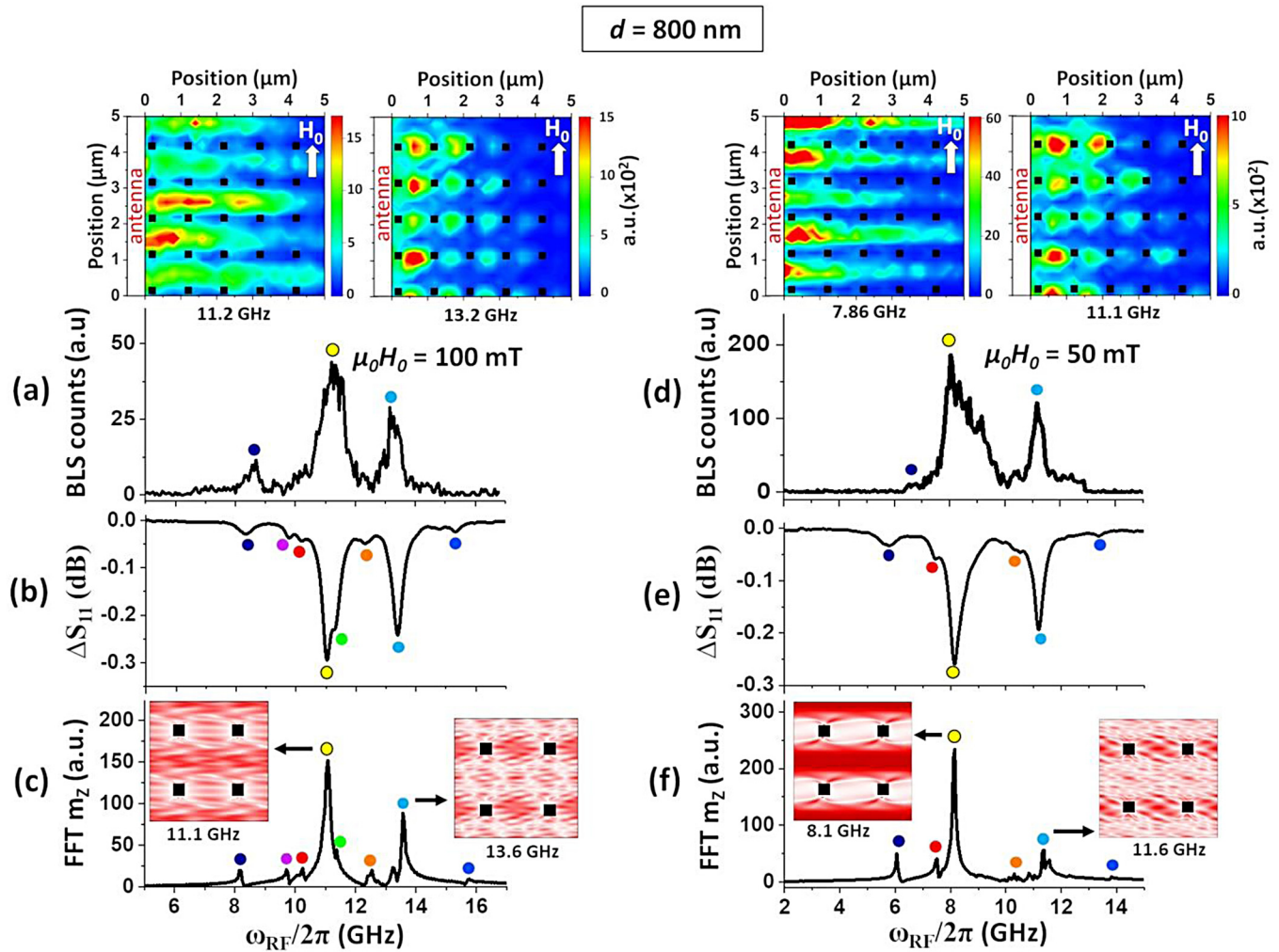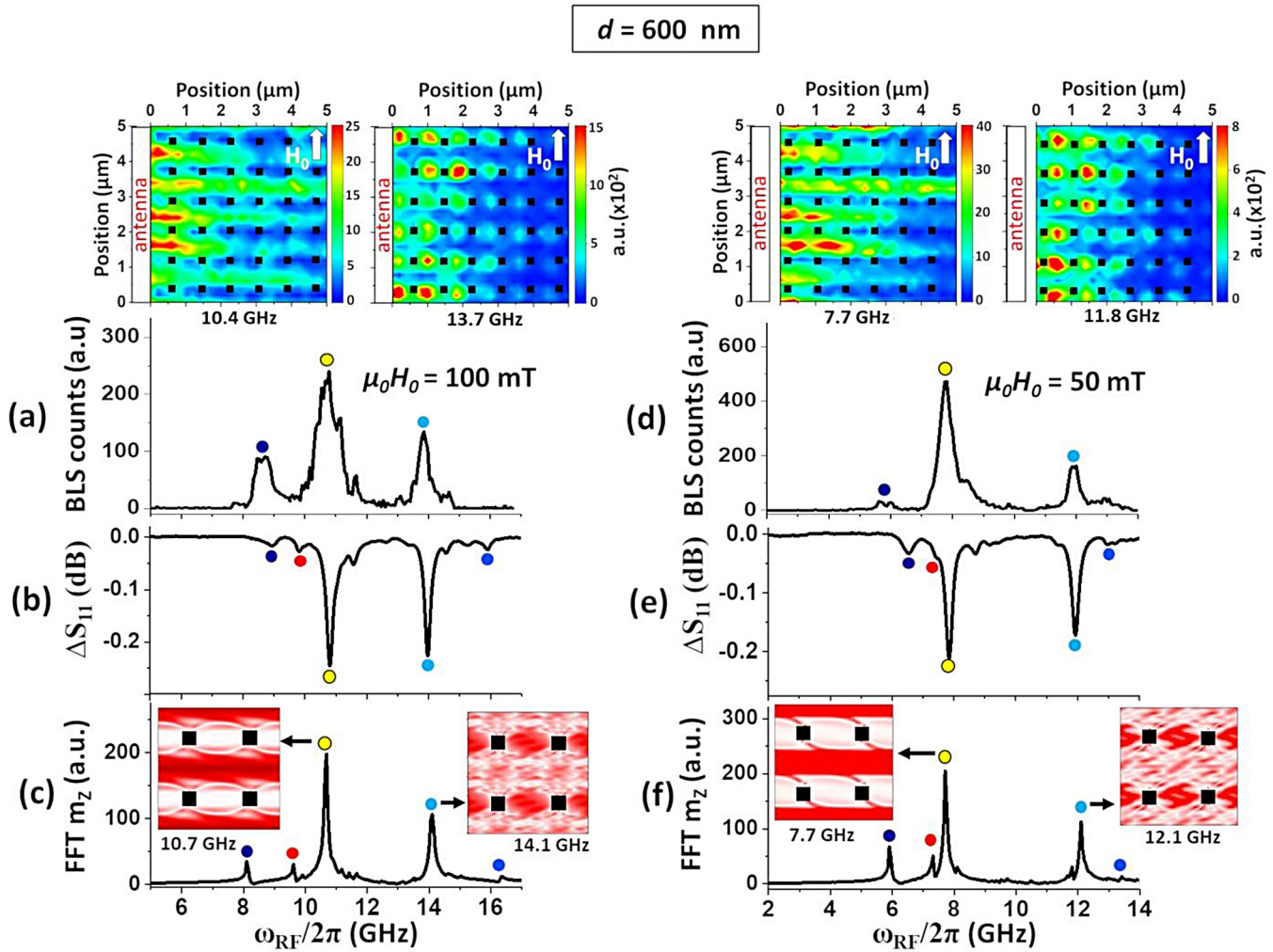
FIG. 5. Spin wave spectra recorded by BLS for $d = 800$ nm at $\mu_0 H_0 = 100$ mT (a) and $\mu_0 H_0 = 50$ mT (d). On top of each spectrum, we present the BLS intensity mapping recorded at the frequencies of the two main modes shown by the yellow and turquoise circles. Frequency-sweep FMR measurements performed for $d = 800$ nm at $\mu_0 H_0 = 100$ mT (b) and $\mu_0 H_0 = 50$ mT (e). FFT spectra calculated for $d = 800$ nm at $\mu_0 H_0 = 100$ mT (c) and $\mu_0 H_0 = 50$ mT (f). The insets in (c) and (f) present the spatial distribution of the calculated FFT amplitude at the frequencies of the two main modes shown by the yellow and turquoise circles. In all panels, the colored symbols are the same as the ones used in Fig. 3.

channels comprised between the rows of antidots and we integrate it over all horizontal channels. Finally, the intensity is normalized by its value at the first pixel position to allow a comparison of decay lengths at different H_0 values. The decay length λ_D of the SW intensity can then be estimated from the fit of the intensity according to the equation,

$$I(x) = \exp\left(-\frac{2x}{\lambda_D}\right) + I_0,\qquad(1)$$

where x is the distance from the antenna and I_0 is the offset intensity.

As reported in Fig. 7, we find that λ_D is comprised in the range between 4 and $6.5\,\mu$m. Note that these values are of the same order of magnitude as the decay lengths observed in YIG waveguides with geometric dimensions similar to those of the channels comprised between the antidots.[76–78] Moreover, the λ_D values do not show a clear tendency on changing d or H_0, indicating that SW propagation is mainly affected by the local geometrical imperfections of the antidot array. Indeed, λ_D is theoretically related to the frequency linewidth at half maximum Δf of the resonance peak by the equation $\lambda_D = 2V_g/\Delta f$, with V_g being the group velocity of the SW mode. In the MC, Δf is higher than in the thin film or bulk material because of the local variation of the internal field due to the antidot shape[35,79] or the SW reflections.[80]

FIG. 6. Spin wave spectra recorded by BLS for $d = 600$ nm at $\mu_0 H_0 = 100$ mT (a) and $\mu_0 H_0 = 50$ mT (d). On top of each spectrum, we present the BLS intensity mapping recorded at the frequencies of the two main modes shown by the yellow and turquoise circles. Frequency-sweep FMR measurements performed for $d = 600$ nm at $\mu_0 H_0 = 100$ mT (b) and $\mu_0 H_0 = 50$ mT (e). FFT spectra calculated for $d = 600$ nm at $\mu_0 H_0 = 100$ mT (c) and $\mu_0 H_0 = 50$ mT (f). The insets in (c) and (f) present the spatial distribution of the calculated FFT amplitude at the frequencies of the two main modes shown by the yellow and turquoise circles. In all panels, the colored symbols are the same as the ones used in Fig. 4.

A rough estimation of V_g of this mode can still be obtained considering as a good approximation the Δf values estimated from the frequency-sweep FMR measurements shown in Figs. 5(b) and 6(b). This leads to V_g of the order of 1.1 and 0.7 km s^{-1} for $d = 800$ and 600 nm, respectively. Let us note that for $d = 800$ nm, while λ_D is different for both H_0 values, V_g is roughly equivalent because the estimation of Δf at $\mu_0 H_0 = 100$ mT is made difficult by the mixing of the yellow and green modes.

C. Spin wave modes at low fields and reconfigurable microwave spectra at remanence

When $\mu_0 H_0$ is decreased below 10 mT and down to the remanence, we observe some major differences between the SW spectra

of the two samples presented in Fig. 2. For example, modes A and B disappear for $d = 600$ nm and many low intensity modes appear in the 2–10 GHz range. In contrast, for $d = 800$ nm, the spectrum shows similar tendencies from the intermediate state down to the remanence. Let us note that for the sake of clarity, we do not report in Fig. 2 the frequency positions of the spin wave modes calculated at remanence.

These differences are related to the cubic crystal anisotropy of CMS, which implies different equilibrium states as a function of d. For 800 nm, the crystal anisotropy allows to keep a large part of the magnetization in the horizontal channel aligned in the direction of H_0, even at remanence. For example, Fig. 8(b) shows the REM Y state corresponding to the magnetic equilibrium configuration
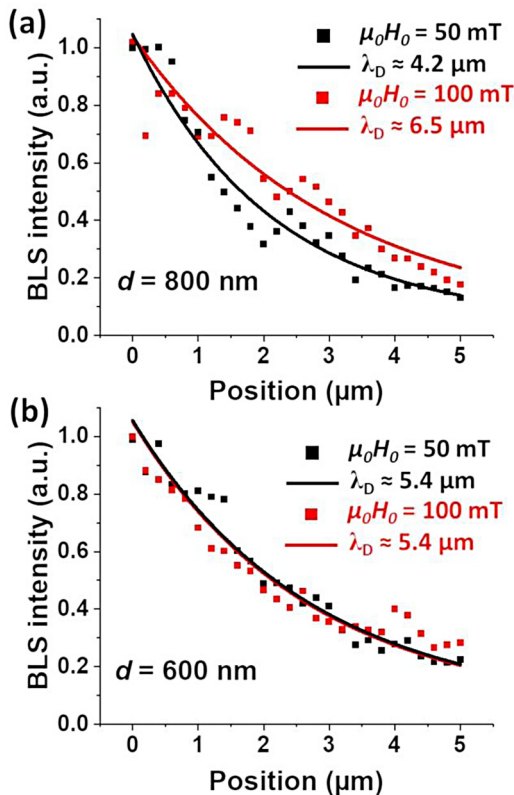
FIG. 7. The evolution of spin wave intensity of the extended mode as a function of the distance x from the antenna for $d =$ (a) 800 and (b) 600 nm. The squares correspond to experimental data and lines correspond to the fit with the value of λ_D given in the figure.

calculated after a saturation field was applied along the y direction. Because edge domains are only a little larger than in the intermediate state, the spatial profile of the 5 main calculated modes are very similar as those calculated at $\mu_0 H_0 = 10$ mT. This is highlighted in Fig. 8(b) with the colored symbols used to sort the SW modes in Fig. 3.

In contrast, for $d = 600$ nm, the cubic anisotropy is not strong enough to counter balance the antidot induced shape anisotropy. Therefore, edge domains continue to spread in the channel until they collapse, leaving magnetic domains, referred to as diagonal domains. Those ones connect diagonally aligned antidots and the magnetization in the domains is roughly aligned at 45° from the x or y axes, as shown by the REM Y state in Fig. 8(d). Therefore, the big change in the FMR spectrum observed in Fig. 2(b) of approximately $\mu_0 H_0 \approx 10$ mT can be explained by the continuously evolving equilibrium state until the diagonal domains are formed. These ones also strongly impact the profiles of the 6 main calculated SWs modes, as shown in Fig. 8(d).

As the cubic anisotropy impacts the CMS remanent states, it can be used to achieve reconfigurable microwave operations at zero field by stabilizing different magnetic configurations after a

saturation field is applied either in the x (REM X) or in the y (REM y) direction. To demonstrate this, for the two samples, we performed frequency-sweep FMR measurements and micromagnetic simulations in the REM Y and REM X states.

For $d = 800$ nm, reconfigurable SW modes are well demonstrated both in the experimental and in the calculated spectra presented in Fig. 8(a). Indeed, we measure 5 main modes in the REM Y state that are strongly extinguished in the REM X state, which are in very good agreement with the calculated spectra. This is because most of the magnetization in the REM X state is parallel to h_{RF}, except in the edge domains where a small part of the magnetic volume can still couple with h_{RF}. The spatial profiles of the SW modes in the REM X state shown in Fig. 8(b) confirm the very weak precession amplitude for all modes except for mode 1, for which the magnetization precession is mainly localized in the edge domains and explains why it is not completely attenuated in the calculated spectrum.

Let us note that even if the frequencies of the calculated and experimental main SW modes agree very well in the REM Y state, we notice that their experimental frequency linewidths are broader than in the simulation. This is attributed to the aforementioned geometrical imperfections of the antidots, which lead to local variations in the equilibrium magnetic configuration. Therefore, we were not able to distinguish experimentally all the low intensity modes expected from the simulations. Also, the ΔS_{11} measurements presented here at remanence are exactly the same if the saturation field is 300 or 10 mT. This allows us to foresee devices with a relatively small reconfigurable field that is required in the context of green technology and low energy consumption devices.

For $d = 600$ nm, the frequency-sweep FMR measurement presented in Fig. 8(c) shows several well-defined SW modes in the REM Y state confirming the small geometrical dispersion of the antidots for this sample. In contrast to the case $d = 800$ nm, we still observe a small signature of some of them in the REM X state. Simulations explain such features by the fact that the magnetization inside the diagonal domains can always couple to h_{RF}. This is observed in Fig. 8(d) where the spatial profiles of the six main modes show a non-negligible precession amplitude in the diagonal domain for the REM X state. As a consequence, the simulated spectra demonstrate that modes 1, 2, 5, and 6 are not expected to be fully attenuated in the REM X state, while modes 3 and 4 and the low intensity modes in between them must be extinguished. Indeed, for these modes, the local π dephasing of the magnetization precession across the sample cancels out the averaged dynamic component.

Therefore, for $d = 600$ nm, we can conclude that the simulations describe qualitatively well the experimental spectra for modes 2–6. They only fail to describe why mode 1 is almost invisible in the frequency-sweep FMR measurement in the REM X state, while the simulations predict only a relatively weak attenuation. For now, we have no clear explanation for this observation. We assume that it is related to the particular spatial profile of this mode in the REM X state. Indeed, the magnetization precession is strong in the domain walls surrounding the diagonal domain. Such walls have shapes and sizes intrinsically very sensitive to even small local variations of geometry around the antidot, which are not considered in our simulations. These variations can lead to a local dephasing of
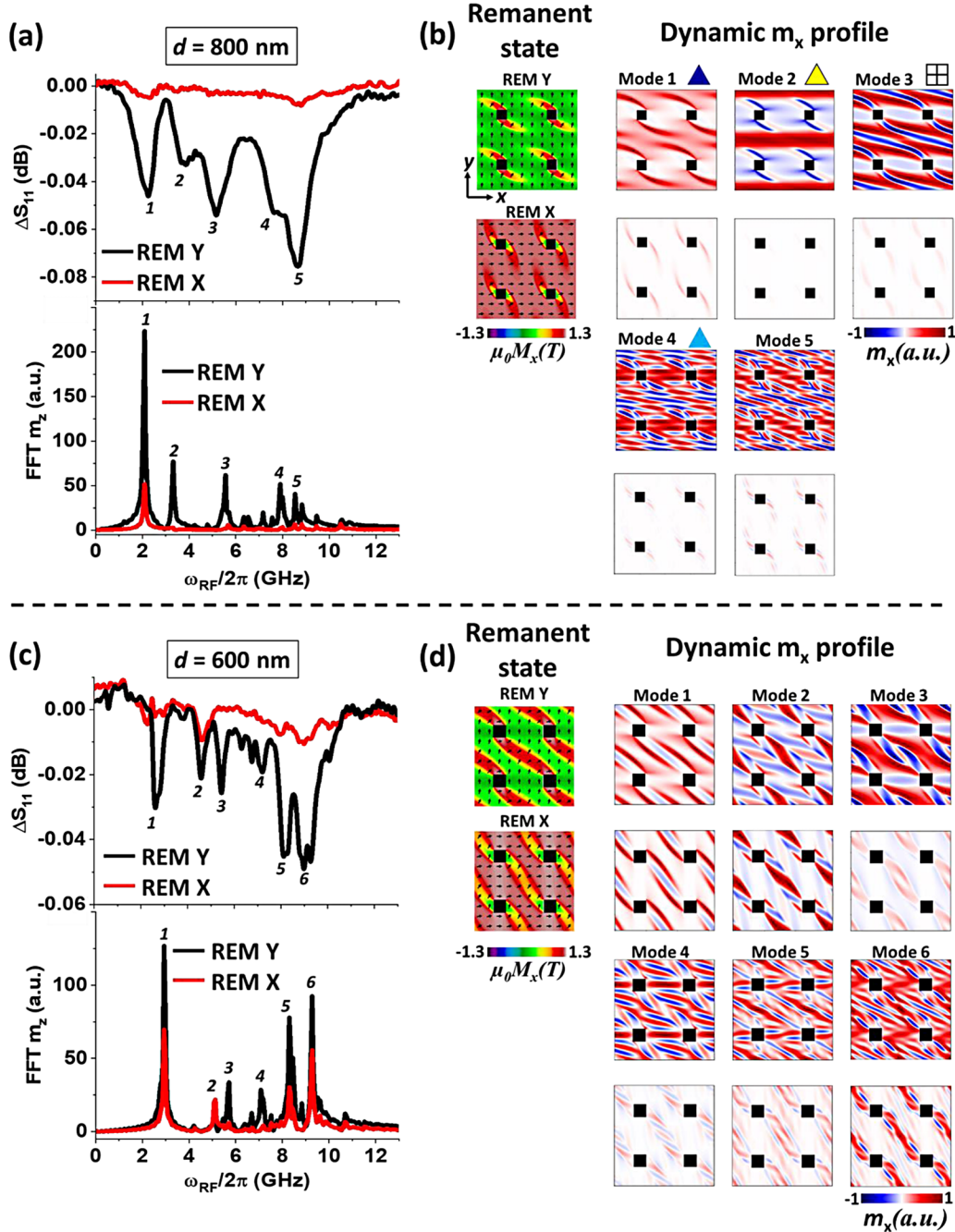
19 February 2024 13:16:43

FIG. 8. Frequency-sweep FMR measurement (top) and calculated FFT spectra (bottom) for the REM Y and REM X remanent states when d = (a) 800 and (c) 600 nm. Simulations for d = (b) 800 and (d) 600 nm of the equilibrium REM Y and REM X states and of the m_x spatial profile of the main dynamic modes numbered in (a) and (c), respectively.

the precession across the sample and then to a decrease of the signal. It is worth mentioning that local variations of the shape and size of the diagonal domains or of the edge domains can also explain why the experimental signal of mode 1 for d = 800 and

600 nm in the REM Y state is not the most intense experimental peak as expected from the simulations.

To find out more about the benefits of using the cubic anisotropy to make reconfigurable microwave operations, even in the case

19 February 2024 13:16:43
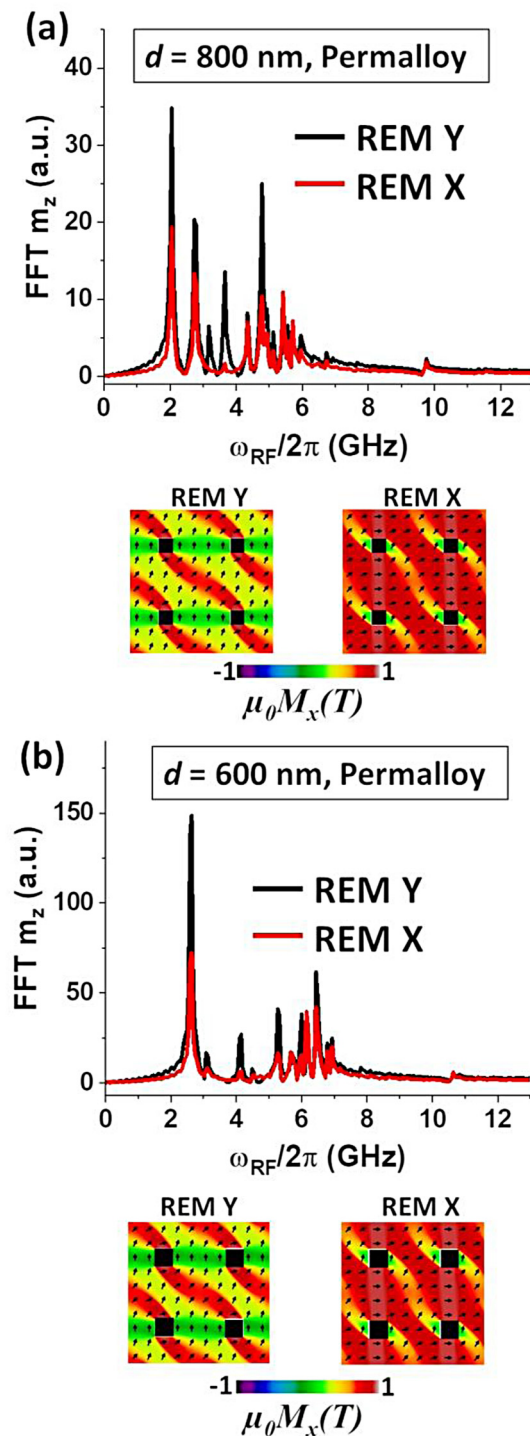
FIG. 9. FFT spectra in the REM Y and REM X remanent states calculated for a MC made of Permalloy with squared antidots with $s = 200$ nm and $d = $ (a) 800 or (b) 600 nm. Below each spectrum is shown the corresponding REM X and REM Y states.

of strongly non-uniform remanent states, we compared the previous FFT spectra calculated for CMS in the REM X and REM Y states with those calculated for a MC having the same geometry but made of Permalloy. Indeed, this magnetic material is widely used both in fundamental studies and in applications. In particular, it presents a magnetization value $\mu_0 M_s = 1$ T that is close to the value for CMS (1.3 T) but has no crystalline anisotropy. Let us note that for the sake of clarity, we performed the micromagnetic simulations with a damping coefficient $\alpha = 2 \times 10^{-3}$ equal to the one used for CMS. But its normal value is about 6×10^{-3}. The results are shown in Fig. 9, where we also present the simulation of the remanent states in the Permalloy MCs.

For $d = 800$ nm, the difference with the spectra of Fig. 8(a) is obvious since most of the dynamic modes are only weakly attenuated in the REM X state. As discussed previously, this is attributed to the presence of diagonal domains for both the REM X and the REM Y states. Such domains are also present for $d = 600$ nm. For this d value, some differences appear with the spectra calculated for CMS. First, only one mode at a frequency of approximately 4 GHz is fully attenuated, whereas at least modes 3 and 4 are attenuated in Fig. 8(c). Second, the modes at high frequencies (≥ 6 GHz) are almost not attenuated at all in the case of Permalloy. We then conclude that the cubic anisotropy of the CMS alloy favors the reconfigurability even in the case of non-uniform remanent states because it favors a more uniform magnetization in the direction of H_0 in the region between the diagonal domains.

For applications, it is interesting to point out that the frequency range of the dynamic modes in CMS (≈ 2–10 GHz) is wider than in Permalloy (≈ 2–8 GHz) at remanence. The possibility of having some part of the channels uniformly magnetized, such as for the sample with $d = 800$ nm in the present work, also favors the propagation of magnetostatic surface spin waves or magnetostatic backward volume waves for frequency filtering applications at remanence, as discussed in Ref. 81.

IV. CONCLUSIONS

In this work, we performed a combined broadband FMR and micro-BLS study of SW modes in MCs made of squared antidots of lateral size 200 nm and spacing 800 or 600 nm etched in a thin film of Co_2MnSi. The experimental results were explained by micromagnetic simulations, which enabled us to calculate the frequency and the spatial profile of each mode, correlating their field evolution with the variation of the magnetic ground state. We demonstrated numerically and experimentally that when the intensity of the static magnetic field is >10 mT, the two main modes with the largest intensity in the spectrum of MCs correspond to a mode localized in the region between the antidots and a propagative mode extending in the channels comprised between the antidots, respectively. For both the samples, the decay length of the extended mode, estimated from micro-BLS measurements, was found to be in order of a few microns, comparable with the values reported for YIG waveguides having geometrical dimensions similar to those of the channels comprised between antidots. Additional modes with lower intensities are also observed, whose number depends on the amplitude of the applied static magnetic field. When the applied magnetic field is <10 mT, the SW spectrum of the samples

19 February 2024 13:16:43

undergoes a strong variation because the edge domains around the antidots spread into the channels. In particular, in the sample with $d = 600$ nm, the edge domains are found to collapse into larger domains connecting antidots aligned diagonally.

Finally, we demonstrated that the cubic anisotropy of the Heusler alloy allows us to obtain a reconfigurable microwave spectrum at remanence. Indeed, it counterbalances the local shape anisotropy induced by the antidots. For a sufficiently large distance between the antidots, it favors quasi-uniform equilibrium remanent states. In particular, for a spacing of 800 nm, we achieved experimentally a very strong attenuation of SW when switching between two perpendicular quasi-uniform states that are not achievable with Permalloy. Such results were very well reproduced by micromagnetic simulations. For smaller antidot spacings leading to a non-uniform equilibrium state, we also observed reconfigurable SW modes in CMS. Their number is higher than that calculated for a MC of the same dimensions in Permalloy, which is again attributed to the cubic anisotropy of the material.

Our study opens some perspectives for the development of reconfigurable multi-band microwave devices based on simple geometry and taking advantage of the intrinsic properties of materials such as crystal anisotropy, which are not usually present in soft materials such as Permalloy.

ACKNOWLEDGMENTS

AUTHOR DECLARATIONS

Conflict of Interest

The authors have no conflicts to disclose.

Author Contributions

S. Mantion: Formal analysis (equal); Investigation (equal); Methodology (equal); Software (equal); Writing – review & editing (equal). **A. Torres Dias:** Investigation (equal); Methodology (equal); Writing – review & editing (equal). **M. Madami:** Data curation (equal); Formal analysis (equal); Investigation (equal); Methodology (equal); Writing – review & editing (equal). **S. Tacchi:** Data curation (equal); Formal analysis (equal); Investigation (equal); Methodology (equal); Writing – original draft (equal); Writing – review & editing (equal). **N. Biziere:** Conceptualization (equal); Data curation (equal); Formal analysis (equal); Funding acquisition (equal); Investigation (equal); Methodology (lead); Software (equal); Writing – original draft (equal); Writing – review & editing (equal).

DATA AVAILABILITY

The data that support the findings of this study are available from the corresponding author upon reasonable request.

REFERENCES

[1]A. V. Chumak, P. Kabos, M. Wu, C. Abert, C. Adelmann, A. O. Adeyeye, J. Åkerman, F. G. Aliev, A. Anane, A. Awad, C. H. Back, A. Barman, G. E. W. Bauer, M. Becherer, E. N. Beginin, V. A. S. V. Bittencourt, Y. M. Blanter, P. Bortolotti, I. Boventer, D. A. Bozhko, S. A. Bunyaev, J. J. Carmiggelt, R. R. Cheenikundil, F. Ciubotaru, S. Cotofana, G. Csaba, O. V. Dobrovolskiy, C. Dubs, M. Elyasi, K. G. Fripp, H. Fulara, I. A. Golovchanskiy, C. Gonzalez-Ballestero, P. Graczyk, D. Grundler, P. Gruszecki, P. Gubbiotti, K. Guslienko, A. Haldar, S. Hamdioui, R. Hertel, B. Hillebrands, T. Hioki, A. Houshang, C.-M. Hu, H. Huebl, M. Huth, E. Iacocca, M. B. Jungfleisch, G. N. Kakazei, A. Khitun, R. Khymyn, T. Kikkawa, M. Kläui, J. W. Kłos, S. Knauer, S. Koraltan, M. Kostylev, M. Krawczyk, I. N. Krivorotov, V. V. Kruglyak, D. Lachance-Quirion, S. Ladak, R. Lebrun, Y. Li, M. Lindner, R. Macêdo, S. Mayr, G. A. Melkov, S. Mieszczak, Y. Nakamura, H. T. Nembach, A. A. Nikitin, S. A. Nikitov, V. Novosad, J. A. Otálora, Y. Otani, A. Papp, B. Pigeau, P. Pirro, W. Porod, F. Porrati, H. Qin, B. Rana, T. Reimann, F. Riente, O. Romero-Isart, A. Ross, A. V. Sadovnikov, A. R. Safin, E. Saitoh, G. Schmidt, H. Schultheiss, K. Schultheiss, A. A. Serga, S. Sharma, J. M. Shaw, D. Suess, O. Surzhenko, K. Szulc, T. Taniguchi, M. Urbánek, K. Usami, A. B. Ustinov, T. van der Sar, S. van Dijken, V. I. Vasyuchka, R. Verba, S. V. Kusminskiy, Q. Wang, M. Weides, M. Weiler, S. Wintz, S. P. Wolski, and X. Zhang, "Advances in magnetics roadmap on spin-wave computing," IEEE Trans. Magn. **58**(6), 1–72 (2022).
[2]A. V. Chumak, V. I. Vasyuchka, A. A. Serga, and B. Hillebrands, "Magnon spintronics," Nat. Phys. **11**(6), 453–461 (2015).
[3]A. Mahmoud, F. Ciubotaru, F. Vanderveken, A. V. Chumak, S. Hamdioui, C. Adelmann, and S. Cotofana, "Introduction to spin wave computing," J. Appl. Phys. **128**(16), 161101 (2020).
[4]B. Lenk, H. Ulrichs, F. Garbs, and M. Münzenberg, "The building blocks of magnonics," Phys. Rep. **507**(4–5), 107–136 (2011).
[5]A. V. Chumak, A. A. Serga, and B. Hillebrands, "Magnon transistor for all-magnon data processing," Nat. Commun. **5**(1), 4700 (2014).
[6]T. Schneider, A. A. Serga, B. Leven, B. Hillebrands, R. L. Stamps, and M. P. Kostylev, "Realization of spin-wave logic gates," Appl. Phys. Lett. **92**(2), 022505 (2008).
[7]K. Szulc, P. Graczyk, M. Mruczkiewicz, G. Gubbiotti, and M. Krawczyk, "Spin-wave diode and circulator based on unidirectional coupling," Phys. Rev. Appl. **14**(3), 034063 (2020).
[8]Q. Wang, M. Kewenig, M. Schneider, R. Verba, F. Kohl, B. Heinz, M. Geilen, M. Mohseni, B. Lägel, F. Ciubotaru, C. Adelmann, C. Dubs, S. D. Cotofana, O. V. Dobrovolskiy, T. Brächer, P. Pirro, and A. V. Chumak, "A magnonic directional coupler for integrated magnonic half-adders," Nat. Electron. **3**(12), 765–774 (2020).
[9]T. Fischer, M. Kewenig, D. A. Bozhko, A. A. Serga, I. I. Syvorotka, F. Ciubotaru, C. Adelmann, B. Hillebrands, and A. V. Chumak, "Experimental prototype of a spin-wave majority gate," Appl. Phys. Lett. **110**(15), 152401 (2017).
[10]H. Arai and H. Imamura, "Neural-network computation using spin-wave-coupled spin-torque oscillators," Phys. Rev. Appl. **10**(2), 024040 (2018).
[11]T. Kampfrath, A. Sell, G. Klatt, A. Pashkin, S. Mährlein, T. Dekorsy, M. Wolf, M. Fiebig, A. Leitenstorfer, and R. Huber, "Coherent terahertz control of antiferromagnetic spin waves," Nat. Photon. **5**(1), 31–34 (2011).
[12]X.-X. Zhang, L. Li, D. Weber, J. Goldberger, K. F. Mak, and J. Shan, "Gate-tunable spin waves in antiferromagnetic atomic bilayers," Nat. Mater. **19**(8), 838–842 (2020).

[13] M. S. Sarker, L. Yao, H. Yamahara, K. Ma, Z. Liao, K. Terao, S. Tang, S. G. Ramaraj, M. Seki, and H. Tabata, "Reconfigurable magnon interference by on-chip dynamic wavelength conversion," Sci. Rep. 13(1), 4872 (2023).

[14] "Magnetochemistry | Free Full-Text | Magnonic crystal with strips of magnetic nanoparticles: Modeling and experimental realization via a dip-coating technique" Magnetochemistry 7, 155 (2021).

[15] R. Mandal, P. Laha, K. Das, S. Saha, S. Barman, A. K. Raychaudhuri, and A. Barman, "Effects of antidot shape on the spin wave spectra of two-dimensional Ni80Fe20 antidot lattices," Appl. Phys. Lett. 103(26), 262410 (2013).

[16] M. Zelent, N. Tahir, R. Gieniusz, J. W. Kłos, T. Wojciechowski, U. Guzowska, A. Maziewski, J. Ding, A. O. Adeyeye, and M. Krawczyk, "Geometrical complexity of the antidots unit cell effect on the spin wave excitations spectra," J. Phys. Appl. Phys. 50(18), 185003 (2017).

[17] J. W. Kłos, D. Kumar, M. Krawczyk, and A. Barman, "Magnonic band engineering by intrinsic and extrinsic mirror symmetry breaking in antidot spin-wave waveguides," Sci. Rep. 3(1), 2444 (2013).

[18] A. V. Chumak, A. A. Serga, B. Hillebrands, and M. P. Kostylev, "Scattering of backward spin waves in a one-dimensional magnonic crystal," Appl. Phys. Lett. 93(2), 022508 (2008).

[19] A. V. Chumak, P. Pirro, A. A. Serga, M. P. Kostylev, R. L. Stamps, H. Schultheiss, K. Vogt, S. J. Hermsdoerfer, B. Laegel, P. A. Beck, and B. Hillebrands, "Spin-wave propagation in a microstructured magnonic crystal," Appl. Phys. Lett. 95(26), 262508 (2009).

[20] A. Adhikari, S. Majumder, Y. Otani, and A. Barman, "Active control of dipole-exchange coupled magnon modes in nanoscale bicomponent magnonic crystals," ACS Appl. Nano Mater. 6(9), 7166–7172 (2023).

[21] J. C. Gartside, A. Vanstone, T. Dion, K. D. Stenning, D. M. Arroo, H. Kurebayashi, and W. R. Branford, "Reconfigurable magnonic mode-hybridisation and spectral control in a bicomponent artificial spin ice," Nat. Commun. 12(1), 2488 (2021).

[22] S. Tacchi, G. Duerr, J. W. Klos, M. Madami, S. Neusser, G. Gubbiotti, G. Carlotti, M. Krawczyk, and D. Grundler, "Forbidden band gaps in the spin-wave spectrum of a two-dimensional bicomponent magnonic crystal," Phys. Rev. Lett. 109(13), 137202 (2012).

[23] K. Szulc, S. Tacchi, A. Hierro-Rodríguez, J. Díaz, P. Gruszecki, P. Graczyk, C. Quirós, D. Markó, J. I. Martín, M. Vélez, D. S. Schmool, G. Carlotti, M. Krawczyk, and L. M. Álvarez-Prado, "Reconfigurable magnonic crystals based on imprinted magnetization textures in hard and soft dipolar-coupled bilayers," ACS Nano 16(9), 14168–14177 (2022).

[24] B. Obry, P. Pirro, T. Brächer, A. V. Chumak, J. Osten, F. Ciubotaru, A. A. Serga, J. Fassbender, and B. Hillebrands, "A micro-structured ion-implanted magnonic crystal," Appl. Phys. Lett. 102(20), 202403 (2013).

[25] A. V. Chumak, T. Neumann, A. A. Serga, B. Hillebrands, and M. P. Kostylev, "A current-controlled, dynamic magnonic crystal," J. Phys. Appl. Phys. 42(20), 205005 (2009).

[26] A. A. Grachev, O. V. Matveev, M. Mruczkiewicz, M. A. Morozova, E. N. Beginin, S. E. Sheshukova, and A. V. Sadovnikov, "Strain-mediated tunability of spin-wave spectra in the adjacent magnonic crystal stripes with piezoelectric layer," Appl. Phys. Lett. 118(26), 262405 (2021).

[27] M. T. Kaffash, S. Lendinez, and M. B. Jungfleisch, "Nanomagnonics with artificial spin ice," Phys. Lett. A 402, 127364 (2021).

[28] K. Zakeri, "Magnonic crystals: Towards terahertz frequencies," J. Phys. Condens. Matter 32(36), 363001 (2020).

[29] G. Gubbiotti, S. Tacchi, M. Madami, G. Carlotti, A. O. Adeyeye, and M. Kostylev, "Brillouin light scattering studies of planar metallic magnonic crystals," J. Phys. Appl. Phys. 43(26), 264003 (2010).

[30] N. I. Polushkin, "Current-induced distortion of the band structure and formation of pseudogaps in magnonic crystals," J. Appl. Phys. 114(3), 033908 (2013).

[31] Q. Wang, Z. Zhong, L. Jin, X. Tang, F. Bai, H. Zhang, and G. S. D. Beach, "Design of nanostrip magnonic crystal waveguides with a single magnonic band gap," J. Magn. Magn. Mater. 340, 23–26 (2013).

[32] A. V. Chumak, A. A. Serga, and B. Hillebrands, "Magnonic crystals for data processing," J. Phys. Appl. Phys. 50(24), 244001 (2017).

[33] P. J. Metaxas, M. Sushruth, R. A. Begley, J. Ding, R. C. Woodward, I. S. Maksymov, M. Albert, W. Wang, H. Fangohr, A. O. Adeyeye, and M. Kostylev, "Sensing magnetic nanoparticles using nano-confined ferromagnetic resonances in a magnonic crystal," Appl. Phys. Lett. 106(23), 232406 (2015).

[34] E. Bankowski, T. Meitzler, R. S. Khymyn, V. S. Tiberkevich, A. N. Slavin, and H. X. Tang, "Magnonic crystal as a delay line for low-noise auto-oscillators," Appl. Phys. Lett. 107(12), 122409 (2015).

[35] R. Zivieri, S. Tacchi, F. Montoncello, L. Giovannini, F. Nizzoli, M. Madami, G. Gubbiotti, G. Carlotti, S. Neusser, G. Duerr, and D. Grundler, "Bragg diffraction of spin waves from a two-dimensional antidot lattice," Phys. Rev. B 85(1), 012403 (2012).

[36] M. Krawczyk and H. Puszkarski, "Plane-wave theory of three-dimensional magnonic crystals," Phys. Rev. B 77(5), 054437 (2008).

[37] A. Haldar, "Functional nanostructures for bias-magnet-free and reconfigurable microwave magnetic devices," Mater. Today Electron. 2, 100008 (2022).

[38] A. Haldar and A. O. Adeyeye, "Functional magnetic waveguides for magnonics," Appl. Phys. Lett. 119(6), 060501 (2021).

[39] A. V. Sadovnikov, G. Talmelli, G. Gubbiotti, E. N. Beginin, S. Sheshukova, S. A. Nikitov, C. Adelmann, and F. Ciubotaru, "Reconfigurable 3D magnonic crystal: Tunable and localized spin-wave excitations in CoFeB meander-shaped film," J. Magn. Magn. Mater. 544, 168670 (2022).

[40] "Making a reconfigurable artificial crystal by ordering bistable magnetic nanowires," Phys. Rev. Lett. 104, 207205 (2010).

[41] "Cubic anisotropy for a reconfigurable magnonic crystal based on ${\mathrm{Co}}_{2}\mathrm{Mn}\mathrm{Si}$ Heusler alloy," Phys. Rev. Appl. 17, 044054 (2022).

[42] A. Haldar and A. O. Adeyeye, "Reconfigurable and self-biased magnonic metamaterials," J. Appl. Phys. 128(24), 240902 (2020).

[43] D. Grundler, "Reconfigurable magnonics heats up," Nat. Phys. 11(6), 438–441 (2015).

[44] C. Guillemard, S. Petit-Watelot, L. Pasquier, D. Pierre, J. Ghanbaja, J.-C. Rojas, A. Bataille, J. Rault, P. L. Fèvre, F. Bertran, and S. Andrieu, "Ultra-low magnetic damping in Co2Mn-based Heusler compounds: Promising materials for spintronic," Phys. Rev. Appl. 11(6), 064009 (2019).

[45] L. J. Singh, "Co2MnSi Heusler alloy thin films," Ph.D. Thesis (University of Cambridge, 2005).

[46] C. Guillemard, W. Zhang, G. Malinowski, C. de Melo, J. Gorchon, S. Petit-Watelot, J. Ghanbaja, S. Mangin, P. Le Fèvre, F. Bertran, and S. Andrieu, "Engineering Co2MnAlxSi1−x Heusler compounds as a model system to correlate spin polarization, intrinsic gilbert damping, and ultrafast demagnetization," Adv. Mater. 32(26), 1908357 (2020).

[47] C. de Melo, C. Guillemard, A. M. Friedel, V. Palin, J. C. Rojas-Sánchez, S. Petit-Watelot, and S. Andrieu, "Unveiling transport properties of Co2MnSi Heusler epitaxial thin films with ultra-low magnetic damping," Appl. Mater. Today 25, 101174 (2021).

[48] I. Abdallah, B. Pradines, N. Ratel-Ramond, G. BenAssayag, R. Arras, L. Calmels, J. F. Bobo, E. Snoeck, and N. Biziere, "Evolution of magnetic properties and damping coefficient of Co 2 MnSi Heusler alloy with Mn/Si and Co/Mn atomic disorder," J. Phys. Appl. Phys. 50(3), 035003 (2017).

[49] I. Galanakis, P. Mavropoulos, and P. H. Dederichs, "Electronic structure and Slater - Pauling behaviour in half-metallic Heusler alloys calculated from first principles," J. Phys. Appl. Phys. 39(5), 765–775 (2006).

[50] S. Andrieu, A. Neggache, T. Hauet, T. Devolder, A. Hallal, M. Chshiev, A. M. Bataille, P. Le Fèvre, and F. Bertran, "Direct evidence for minority spin gap in the Co2MnSi Heusler compound," Phys. Rev. B 93(9), 094417 (2016).

[51] C. Guillemard, S. Petit-Watelot, J.-C. Rojas-Sánchez, J. Hohlfeld, J. Ghanbaja, A. Bataille, P. Le Fèvre, F. Bertran, and S. Andrieu, "Polycrystalline Co2 Mn-based Heusler thin films with high spin polarization and low magnetic damping," Appl. Phys. Lett. 115(17), 172401 (2019).

[52] V. E. Demidov, S. Urazhdin, A. Anane, V. Cros, and S. O. Demokritov, "Spin–orbit-torque magnonics," J. Appl. Phys. 127(17), 170901 (2020).

19 February 2024 13:16:43

[53] J. Thoene, S. Chadov, G. Fecher, C. Felser, and J. Kübler, "Exchange energies, Curie temperatures and magnons in Heusler compounds—IOPscience" J. Phys. Appl. Phys. **42**(8), 084013 (2009).

[54] J. Kübler, "*Ab initio* estimates of the Curie temperature for magnetic compounds," J. Phys. Condens. Matter **18**(43), 9795–9807 (2006).

[55] G. Ortiz, A. García-García, N. Biziere, F. Boust, J. F. Bobo, and E. Snoeck, "Growth, structural, and magnetic characterization of epitaxial Co2MnSi films deposited on MgO and Cr seed layers," J. Appl. Phys. **113**(4), 043921 (2013).

[56] T. Sebastian, Y. Ohdaira, T. Kubota, P. Pirro, T. Brächer, K. Vogt, A. A. Serga, H. Naganuma, M. Oogane, Y. Ando, and B. Hillebrands, "Low-damping spin-wave propagation in a micro-structured Co$_2$Mn$_{0.6}$Fe$_{0.4}$Si Heusler waveguide," Appl. Phys. Lett. **100**(11), 112402 (2012).

[57] T. Stückler, C. Liu, T. Liu, H. Yu, F. Heimbach, J. Chen, J. Hu, S. Tu, Y. Zhang, S. Granville, M. Wu, Z.-M. Liao, D. Yu, and W. Zhao, "Ultrabroadband spin-wave propagation in Co 2 (Mn 0.6 Fe 0.4) Si thin films," Phys. Rev. B **96**(14), 144430 (2017).

[58] S. Wang, J. Ding, X. Guan, M. B. Jungfleisch, Z. Zhang, X. Wang, W. Gu, Y. Zhu, J. E. Pearson, X. Cheng, A. Hoffmann, and X. Miao, "Linear and nonlinear spin-wave dynamics in ultralow-damping microstructured Co2FeAl Heusler waveguide," Appl. Phys. Lett. **113**(23), 232404 (2018).

[59] T. Sebastian, T. Brächer, P. Pirro, A. A. Serga, B. Hillebrands, T. Kubota, H. Naganuma, M. Oogane, and Y. Ando, "Nonlinear emission of spin-wave caustics from an edge mode of a microstructured Co 2 Mn 0.6 Fe 0.4 Si waveguide," Phys. Rev. Lett. **110**(6), 067201 (2013).

[60] P. Pirro, T. Sebastian, T. Brächer, A. A. Serga, T. Kubota, H. Naganuma, M. Oogane, Y. Ando, and B. Hillebrands, "Non-Gilbert-damping mechanism in a ferromagnetic Heusler compound probed by nonlinear spin dynamics," Phys. Rev. Lett. **113**(22), 227601 (2014).

[61] S. Mallick, S. Mondal, T. Seki, S. Sahoo, T. Forrest, F. Maccherozzi, Z. Wen, S. Barman, A. Barman, K. Takanashi, and S. Bedanta, "Tunability of domain structure and magnonic spectra in antidot arrays of Heusler alloy," Phys. Rev. Appl. **12**(1), 014043 (2019).

[62] M. Langer, K. Wagner, T. Sebastian, R. Hübner, J. Grenzer, Y. Wang, T. Kubota, T. Schneider, S. Stienen, K. Lenz, H. Schultheiß, J. Lindner, K. Takanashi, R. E. Arias, and J. Fassbender, "Parameter-free determination of the exchange constant in thin films using magnonic patterning," Appl. Phys. Lett. **108**(10), 102402 (2016).

[63] G. Ortiz, A. Garcia, J. B. Youssef, N. Biziere, F. Boust, J.-F. Bobo, E. Snoeck, and N. Vukadinovic, "Broadband ferromagnetic resonance study of Co2MnSi thin films: Effect of the film thickness," IEEE Trans. Magn. **49**(3), 1037–1040 (2013).

[64] B. A. Kalinikos, M. P. Kostylev, N. V. Kozhus, and A. N. Slavin, "The dipole-exchange spin wave spectrum for anisotropic ferromagnetic films with mixed exchange boundary conditions," J. Phys. Condens. Matter **2**(49), 9861 (1990).

[65] A. Vansteenkiste and B. Van de Wiele, "MuMax: A new high-performance micromagnetic simulation tool," J. Magn. Magn. Mater. **323**(21), 2585–2591 (2011).

[66] A. Vansteenkiste, J. Leliaert, M. Dvornik, M. Helsen, F. Garcia-Sanchez, and B. Van Waeyenberge, "The design and verification of MuMax3," AIP Adv. **4**(10), 107133 (2014).

[67] S. Neusser, B. Botters, M. Becherer, D. Schmitt-Landsiedel, and D. Grundler, "Spin-wave localization between nearest and next-nearest neighboring holes in an antidot lattice," Appl. Phys. Lett. **93**(12), 122501 (2008).

[68] S. Neusser, B. Botters, and D. Grundler, "Localization, confinement, and field-controlled propagation of spin waves in Ni 80 Fe 20 antidot lattices," Phys. Rev. B **78**(5), 054406 (2008).

[69] C. Yu, M. J. Pechan, and G. J. Mankey, "Dipolar induced, spatially localized resonance in magnetic antidot arrays," Appl. Phys. Lett. **83**(19), 3948–3950 (2003).

[70] J. Sklenar, V. S. Bhat, L. E. DeLong, O. Heinonen, and J. B. Ketterson, "Strongly localized magnetization modes in permalloy antidot lattices," Appl. Phys. Lett. **102**(15), 152412 (2013).

[71] M. J. Pechan, C. Yu, R. L. Compton, J. P. Park, and P. A. Crowell, "Direct measurement of spatially localized ferromagnetic-resonance modes in an antidot lattice (invited)," J. Appl. Phys. **97**(10), 10J903 (2005).

[72] S. Tacchi, M. Madami, G. Gubbiotti, G. Carlotti, A. Adeyeye, S. Neusser, B. Botters, and D. Grundler, "Magnetic normal modes in squared antidot array With circular holes: A combined Brillouin light scattering and broadband ferromagnetic resonance study," Magn. IEEE Trans. On **46**, 172–178 (2010).

[73] S. Tacchi, G. Gubbiotti, M. Madami, and G. Carlotti, "Brillouin light scattering studies of 2D magnonic crystals," J. Phys. Condens. Matter **29**(7), 073001 (2017).

[74] S. Mantion and N. Biziere, "Influence of Ga$^+$ milling on the spin waves modes in a Co$_2$ MnSi Heusler magnonic crystal," J. Appl. Phys. **131**(11), 113905 (2022).

[75] S. Tacchi, P. Gruszecki, M. Madami, G. Carlotti, J. W. Kłos, M. Krawczyk, A. Adeyeye, and G. Gubbiotti, "Universal dependence of the spin wave band structure on the geometrical characteristics of two-dimensional magnonic crystals," Sci. Rep. **5**(1), 10367 (2015).

[76] B. Heinz, Q. Wang, M. Schneider, E. Weiß, A. Lentfert, B. Lägel, T. Brächer, C. Dubs, O. V. Dobrovolskiy, P. Pirro, and A. V. Chumak, "Long-range spin-wave propagation in transversely magnetized nano-scaled conduits," Appl. Phys. Lett. **118**(13), 132406 (2021).

[77] B. Heinz, T. Brächer, M. Schneider, Q. Wang, B. Lägel, A. M. Friedel, D. Breitbach, S. Steinert, T. Meyer, M. Kewenig, C. Dubs, P. Pirro, and A. V. Chumak, "Propagation of spin-wave packets in individual Nanosized yttrium iron garnet magnonic conduits," Nano Lett. **20**(6), 4220–4227 (2020).

[78] H. Merbouche, M. Collet, M. Evelt, V. E. Demidov, J. L. Prieto, M. Muñoz, J. Ben Youssef, G. de Loubens, O. Klein, S. Xavier, O. D'Allivy Kelly, P. Bortolotti, V. Cros, A. Anane, and S. O. Demokritov, "Frequency filtering with a magnonic crystal based on nanometer-thick yttrium iron garnet films," ACS Appl. Nano Mater. **4**(1), 121–128 (2021).

[79] S. Mantion and N. Biziere, "Influence of Ga+ milling on the spin waves modes in a Co2MnSi Heusler magnonic crystal," J. Appl. Phys. **131**(11), 113905 (2022).

[80] V. V. Kruglyak and A. N. Kuchko, "Damping of spin waves in a real magnonic crystal," J. Magn. Magn. Mater. **272–276**, 302–303 (2004).

[81] S. Mantion and N. Biziere, "Cubic anisotropy for a reconfigurable magnonic crystal based on Co 2 Mn Si Heusler alloy," Phys. Rev. Appl. **17**(4), 044054 (2022).